metals

MDPI

Article

Comparison of Conventional and Flash Spark Plasma Sintering of Cu–Cr Pseudo-Alloys: Kinetics, Structure, Properties

Kirill V. Kuskov [1,*], Mohammad Abedi [1], Dmitry O. Moskovskikh [1], Illia Serhiienko [2] and Alexander S. Mukasyan [3,*]

[1] Center of Functional Nanoceramics, National University of Science and Technology MISiS, 119049 Moscow, Russia; abedi_muhammad@yahoo.com (M.A.); mos@misis.ru (D.O.M.)
[2] Academic Research Center for Energy Efficiency, National University of Science and Technology MISiS, 119049 Moscow, Russia; sergienko208@gmail.com
[3] Department of Chemical and Biomolecular Engineering, University of Notre Dame, Notre Dame, IN 46556, USA
* Correspondence: kkuskov@misis.ru (K.V.K.); amoukasi@nd.edu (A.S.M.); Tel.: +7-495-955-0113 (K.V.K.); +1-574-631-9825 (A.S.M.)

Abstract: Spark plasma sintering (SPS) is widely used for the consolidation of different materials. Copper-based pseudo alloys have found a variety of applications including as electrodes in vacuum interrupters of high-voltage electric circuits. How does the kinetics of SPS consolidation for such alloys depend on the heating rate? Do SPS kinetics depend on the microstructure of the media to be sintered? These questions were addressed by the investigation of SPS kinetics in the heating rate range of 0.1 to 50 K/s. The latter conditions were achieved through flash spark plasma sintering (FSPS). We also compared the sintering kinetics for the conventional copper–chromium mixture and for the mechanically induced copper/chromium nanostructured particles. It was shown that, under FSPS conditions, the observed maximum consolidation rates were 20–30 times higher than that for conventional SPS with a heating rate of 100 K/min. Under the investigated conditions, the sintering rate for mechanically induced composite Cu/Cr particles was 2–4 times higher compared to the conventional Cu + Cr mixtures. The apparent sintering activation energy for the Cu/Cr powder was twice less than that for Cu–Cr mixture. It was concluded that the FSPS of nanostructured powders is an efficient approach for the fabrication of pseudo-alloys.

Keywords: pseudo-alloys; spark plasma sintering; flash spark plasma sintering; kinetics

Citation: Kuskov, K.V.; Abedi, M.; Moskovskikh, D.O.; Serhiienko, I.; Mukasyan, A.S. Comparison of Conventional and Flash Spark Plasma Sintering of Cu–Cr Pseudo-Alloys: Kinetics, Structure, Properties. *Metals* **2021**, *11*, 141. https://doi.org/10.3390/met11010141

Received: 6 November 2020
Accepted: 7 January 2021
Published: 12 January 2021

1. Introduction

Copper-based composites, which involve immiscible elements (e.g., Cr, W, Mo), so-called pseudo-alloys, have attracted a vast of attention for a variety of applications including a new generation of electrical contacts, electrodes for point welding, and radiators, etc. [1–6]. Due to a unique combination of thermal, electrical, and mechanical properties as well as being corrosion resistant under applied high-voltage, such materials have found specific use as the electrodes in vacuum interrupters of high-voltage electric circuits [7]. New approaches of powder metallurgy such as additive manufacturing technologies [8–10], spark plasma sintering (SPS) [3,4,11], self-propagating high-temperature synthesis (SHS) [5], and high energy ball milling (HEBM) [1,3,4,11–15] permit control of the microstructure of such pseudo-alloys, and hence significantly improve their properties [16–21]. For example, by optimizing the parameters of HEBM, one may obtain composite nanostructured particles with different sizes of the metal constituents with the formation of supersaturated solid solutions [3,8,13–15,22], which cannot be produced by conventional methods. Furthermore, control of the alloys' structure takes place during the consolidation stage. The SPS method allows for a precise variation of the sintering parameters, specifically including the preheating rates. There are a vast number of publications, both theoretical [23–26] and experimental [27–29], on the SPS of different ceramics

and alloys, while much less works have reported the consolidation of the pseudo-alloys. Additionally, the influence of heating rates on the SPS kinetics is not well understood. In this work, we report the results on the consolidation kinetics of the Cu–Cr pseudo alloys, in a wide range of heating rates including the so-called, flash SPS mode [30], with heating rates up to 50 K/s. We also compared the SPS kinetics for the conventional Cu + Cr mixture and composite Cu/Cr nanostructured particles fabricated by the HEBM method.

2. Materials and Methods

2.1. Precursors

Commercial Cu powder (99.97, particle size <60 μm) with a dendrite type of morphology (Figure 1a) and Cr powder (99.7, average particle size 25 μm) with elongated faceted morphology (Figure 1b) were used as the precursors.

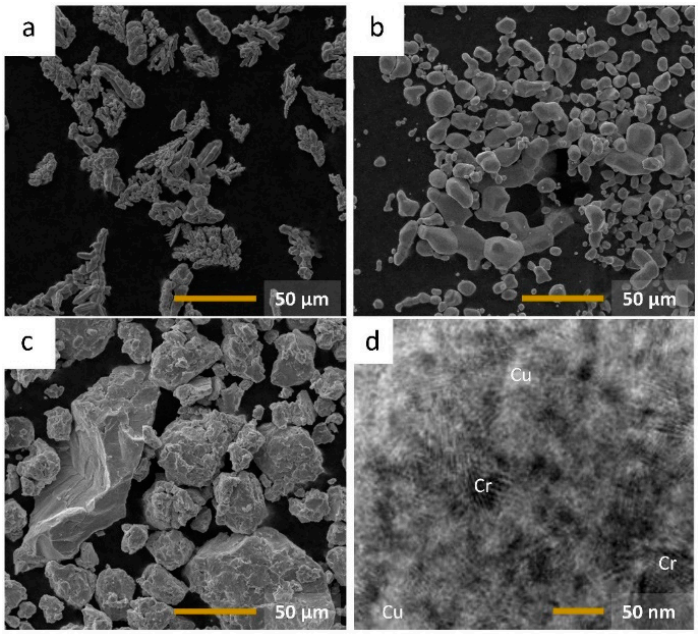

Figure 1. Microstructures: the raw powders Cu (**a**), Cr (**b**); the mechanically induced particles' scanning electron microscope (SEM) image (**c**); transmission electron microscope (TEM) image (**d**).

2.2. Ball Mixing and Milling

Powders were mixed and milled in the proportion 55 wt.% of Cu and 45 wt.% of Cr. For conventional mixing, the Wise Mix BML-2 BML-6 (South Korea) machine was used. Precursors in the desired weight ratio were put into the jar and subjected to mixing for 12 h with a rotating speed of 175 rpm. Here and after, the mixture, which was prepared by this procedure, was named "Cu + Cr".

The planetary ball mill Activator-2S (Russia) was also employed for the milling of the precursor. Copper and chromium powders with the above-mentioned desired ratio were placed into the stainless steel jars. A ball to powder ratio of 20:1 was utilized, and the average diameter of the stainless steel balls was 7 mm. The jars were vacuumed, and filled up to 0.4 MPa with highly pure argon. This process was repeated three times to ensure that the entire volume of the container was filled with pure argon. The mixtures underwent HEBM with a sun wheel rotating speed of 694 rpm and jar rotating speed of 694 rpm. The jars were water-cooled continuously during HEBM. The powders were milled for 15 min increments followed by 5 min of cooling time, for a total milling time of 60 min. Figure 1c,d illustrates the morphology of the powders after the HEBM treatment. It can be seen that after HEBM, the size of the particles increased as compared to the initial precursors due to the cold-welding phenomenon and was in the range of 2–100 μm with an average size of ~35 μm (Figure 1c). However, each particle fabricated by HEBM involves

both Cu and Cr mixed on the nanostructure level (Figure 1d). Hereafter, this powder was named as the nanostructured "Cu/Cr" composite particles.

2.3. Consolidation Schemes

The consolidation experiments were performed in the Labox 650 (SinterLand, Nagaoka, Japan) SPS installation. The DC pulse patterns used were 40 ms-ON and 7 ms-OFF. All experiments were carried out in vacuum (~10 Pa). The sample temperature was measured by a K-type thermocouple. Temperature, applied force, current, voltage, displacement, and vacuum pressure of the SPS chamber were registered during the experiments. The axial displacements of the samples were recorded at 1 s time intervals with a precision of 1 μm. The thermal expansion of the graphite tools was subtracted from the raw displacement values to obtain the actual densification of the samples. The cylindrical graphite dies used in this work had an internal diameter in the range of 13–15 mm, an outer diameter of 30 mm, and a 30 mm height. For each experiment, the desired mixture was placed into the die and initially cold pressed under a load of 50 MPa. The relative densities of the compacts before the preheating stage were 55 ± 1% and 65 ± 1% for the nanostructured Cu/Cr particles and Cu + Cr mixtures, respectively.

Two schemes were used for the consolidation of powder compacts (i.e., conventional spark plasma sintering (SPS) and flash spark plasma sintering (FSPS)). The schemes of the sintering profiles are shown in Figure S1. In the SPS scheme (Figure S1a), the sample was wrapped with graphite paper and inserted inside the die. In this case, the current circulated in both the graphite tool and the powder compact. Four different sintering temperatures (i.e., 923, 973, 1048, and 1123 K) were used to investigate the consolidation kinetics. The dwelling time for all experiments was 10 min. The heating rate for all selected temperatures was 100 K/min, except 973 K, where both 5 and 100 K/min were evaluated in order to study the effect of heating rates on the kinetics of sintering at the same temperature.

In the FSPS scheme (Figure S1b), the inner surface of the die was coated with electrical insulated material (i.e., hexagonal boron nitride) with a thickness of 0.2 ± 0.05 mm to prevent transmission of the DC pulses through the die and concentrating the entire current on the sample and graphite paper. The electrical insulation between the graphite die and the punches was verified, before and after each experiment by the multimeter (see [31] for more details). The temperature was increased manually at 100 K/min to 473 K, followed by rapid increase of the electrical current to the predetermined value in 5 s and kept for 10 s (see Figure S1b). Such an electrical current pattern is called "the forced mode" [30]. Thus, in the FSPS scheme, the maximum temperature was not pre-selected, but measured as a function of the applied current.

We also used two different schedules for the applied pressure. Plan A, where the pressure of 50 MPa was applied at room temperature and kept constant until the end of sintering procedure and Plan B, where the pressure of 0.1 MPa was applied at room temperature kept up to 473 K, followed by its rapid increase to 50 MPa and the value was kept constant until the end of the experiment.

Table S1 summarizes the experimental conditions for the different experiments. The designation W_X_Y_Z was employed for identification of the samples, where "W" represents the scheme of sintering (SPS or FSPS), "X" indicates the type of raw powder that used (Cu + Cr or Cu/Cr), and "Y" denotes the sintering temperature in the case of the SPS test and maximum recorded temperature in the case of the FSPS experiments. Finally, "Z" indicates the type of applied pressure plan (A or B).

2.4. Characterization

The microstructure of the materials was studied using scanning electron microscopy (SEM, JSM-7600F, JEOL, Tokyo, Japan) equipped with an EDS spectrometer (Oxford Instruments X-MAX 80) as well as the transmission electron microscope (TEM, TITAN 800–300, FEI, Oregon, OR, USA). Image processing software (ImageJ 1.52v, National Institutes

of Health, Bethesda, MD, USA and Photoshop CS6, 22.1.0, Adobe, San José, CA, USA) was utilized for the analysis of the microstructural parameters. The relative density (Δ) of the sample was calculated based on the measurements of the mass (m) and the volume (cylinder with constant diameter, d, and the height h; $V = \pi d^2 \cdot h$) of the sample and the knowledge of the theoretical density (ρ_{th}) of the considered composition of the mixture: $\Delta = (m/V)/\rho_{th}$. In the case of the immiscible Cu–Cr alloy, we assumed that ρ_{th} = const. The diameter (d) and the height (h) of the sample was measured with an accuracy of 1 μm. The volume of the sintered samples was also measured by the Archimedes' method.

For specific electrical resistance measurements, samples were cut into rectangular cubes with the dimensions of about 11 mm × 5 mm × 0.2 mm. The four-contact method at the DC was employed in a setup provided by KRIOTEL Ltd. (Moscow, Russia). At least five measurements were performed to obtain the average values of the specific electrical resistivity and corresponding standard deviations. The thermal diffusivity of the materials was measured by the laser flash method on a thermal diffusivity analyzer LFA457 NETZSCH (Selb, Germany). For this experiment, cylindrical pieces with a diameter of 12.7 mm and a height of 1.5 to 2 mm were used. For each sample, the test was repeated five times.

The mechanical properties of the sintered samples including the hardness and elastic modulus were measured on the polished micro-sections using a Micro-Hardness Tester (CSM Instruments, Peuseux, Switzerland) by the Oliver and Farr method, which allowed us to determine these characteristics by analyzing the resulting load–displacement curves. A diamond pyramid was used as the indenter (Vickers hardness test), the maximum load was 100 mN, and the duration of a single loading–unloading cycle was 72 s.

3. Results and Discussion

3.1. Spark Plasma Sintering: Kinetics

Two types of mixtures (i.e., conventionally blended Cu + Cr powders and mechanically induced nanostructured Cu/Cr particles) were subjected to SPS under different temperature–time schedules (Table 1). The load of Plan A and dwelling time (10 min) were used for this set of conventional SPS experiments.

Table 1. Some kinetics parameters for the spark plasma sintering (SPS) of different consolidated media.

SPS Conditions T_{max} Heating Rate	Type of Powder Mixture	Final Relative Density, %	n Isothermal Conditions	Ave. $d\chi/dt$ Preheating Stage, 10^{-3} s^{-1}	Ave. $d\chi/dT$ Preheating Stage 10^{-5} s^{-1}
923 K, 100 K/min	Cu + Cr	80 ± 0.2	0.45 ± 0.05	1.0 ± 0.1	1.0
	Cu/Cr	93 ± 0.5	0.5 ± 0.03	3.1 ± 0.4	3.1
973 K, 100 K/min	Cu + Cr	85 ± 0.2	0.5 ± 0.04	1.0 ± 0.1	1.0
	Cu/Cr	96 ± 0.5	0.5 ± 0.05	3.1 ± 0.4	3.1
1023 K, 100 K/min	Cu + Cr	91 ± 0.2	0.48 ± 0.03	1.0 ± 0.1	1.0
	Cu/Cr	98 ± 0.2	0.5 ± 0.05	3.1 ± 0.4	3.1
1023 K, 100 K/min	Cu + Cr	93 ± 0.2	0.4 ± 0.05	1.0 ± 0.1	1.0
	Cu/Cr	99 ± 0.5	0.4 ± 0.05	3.1 ± 0.4	3.1
973 K, 5 K/min	Cu + Cr	83.8 ± 0.2	0.5 ± 0.04	0.044	0.88
	Cu/Cr	94.5 ± 0.3	0.5 ± 0.03	0.167	3.34

The typical dependences of the relative sample's density (Δ) versus temperature (T) for Cu + Cr and Cu/Cr mixtures are shown in Figure 2a,b, respectively. Several qualitative conclusions can be made. First, it can be seen that the initial densities (Δ_0) of the compacted (50 MPa) powders were different for the mixtures. The conventionally mixed Cu + Cr samples had Δ_0 in the range of 66–67%, while Δ_0 for the Cu/Cr composite particles was 53–55%. This means that the compressibility of the mechanically induced particles at room temperature was less that for the conventional mixture. Second, considering that the heating rate was the same (100 K/min) for both media, it may be implied that the sintering rate

for the Cu/Cr media was much higher compared to the conventional mixture. As a result, the final densities of the compacted materials were higher for the nanostructured Cu/Cr particles (see Table 1).

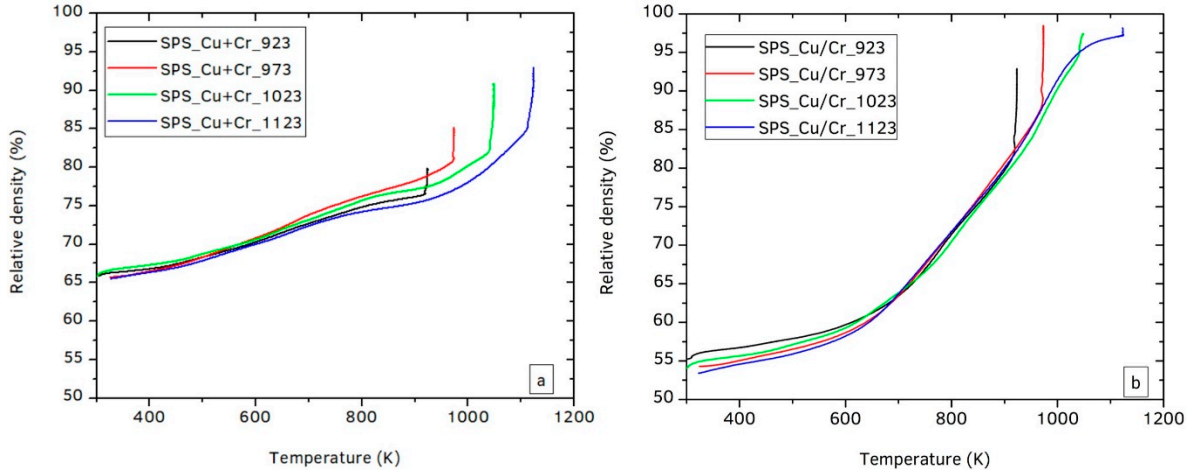

Figure 2. Typical dependences of relative density vs. temperature for the (**a**) conventional Cu + Cr mixture; (**b**) and Cu/Cr particles (spark plasma sintering (SPS) conditions: 100 K/min, Plan A).

For quantitative analysis of the obtained data, let us introduce the so-called densification parameter (χ) as follows [32]:

$$\chi = \frac{\rho_{in} - \rho_0}{\rho_{th} - \rho_0} \quad (1)$$

where ρ_0, ρ_{in}, and ρ_{th} correspond to the initial density, instantaneous density at a given time, and theoretical density of the sample, respectively. The kinetic functions $\chi = F(t)$ for the Cu + Cr and Cu/Cr media sintered up to different maximum temperatures are shown in Figure 3a,b correspondingly.

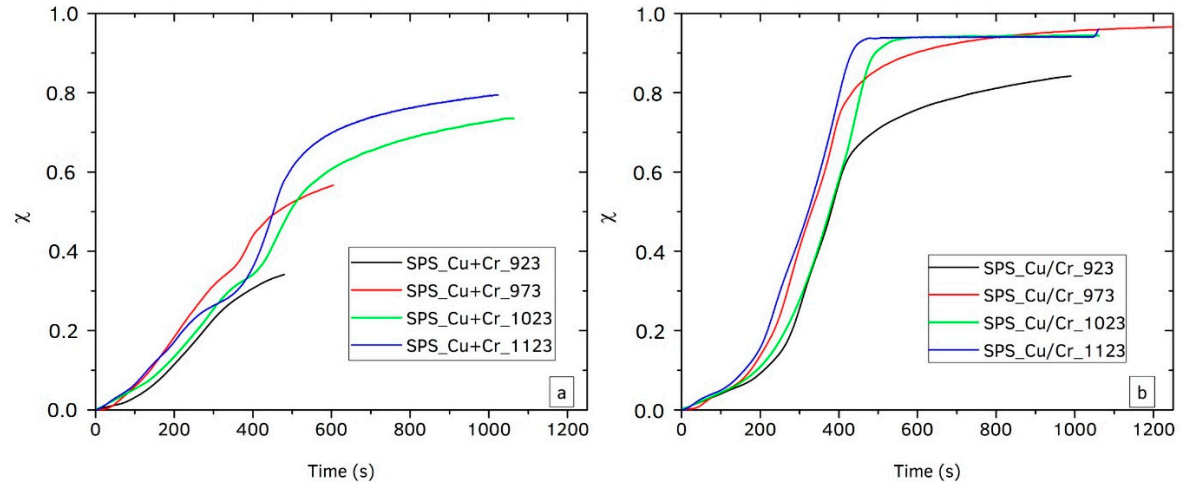

Figure 3. Typical consolidation kinetics for the (**a**) conventional Cu + Cr mixture and (**b**) Cu/Cr particles (SPS conditions: 100 K/min, Plan A).

For further analysis, let us use the widely recognized phenomenological sintering equation [32–34]:

$$\chi = kt^n \quad (2)$$

where k is the linear parameter and n is the time exponent of the sintering equation. Parameter k is typically presented as follows:

$$k = k_0 e^{-Q/RT} \tag{3}$$

where k_0 is the pre-exponential factor and Q is the effective activation energy of the sintering process.

According to Equations (2) and (3) under isothermal conditions (k = const), we have a linear dependence:

$$ln\chi = lnk + nlnt \tag{4}$$

where a slope is a value of parameter n.

The corresponding treatment of the experimental data showed that, indeed, with high accuracy (Adj. R square 0.97–0.99), all experimentally obtained kinetic dependences could be fit by the linear function (4) with the n value varied in the range of 0.4–0.5 (Table 1). Knowing the n values, the Arrhenius plots were used to estimate the apparent activation energy (Q) of the consolidation process for different sintering media:

$$\frac{ln\chi}{t^n} = lnk_o - \frac{Q}{RT} \tag{5}$$

These plots are shown in Figure 4. It can be seen that the conventional Cu + Cr mixture had $Q_{Cu+Cr} = 12{,}271 \cdot R = 102 \pm 15$ kJ/mol, while Q for the nanostructured Cu/Cr particles was more than twice smaller (i.e., $Q_{Cu/Cr} = 5571 \cdot R = 46 \pm 2$ kJ/mol).

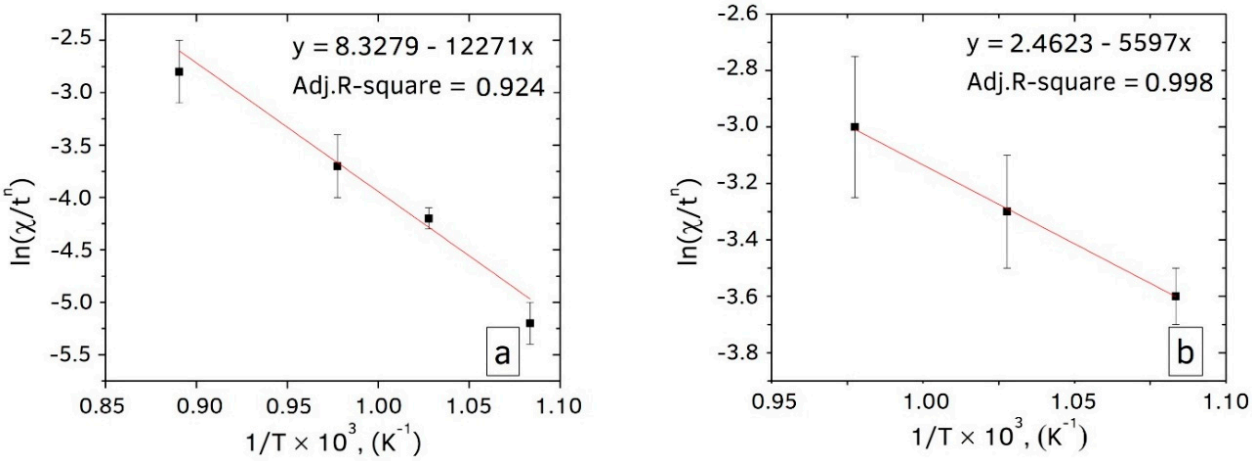

Figure 4. Arrhenius plots for (**a**) the Cu + Cr mixture and (**b**) Cu/Cr particles (SPS conditions: 100 K/min, 50 MPa).

For the non-isothermal sintering conditions, we may re-write Equation (2) as follows:

$$\frac{d\chi}{dt} = nt^{n-1}k + t^n\frac{dk}{dt} = t^n k\frac{n}{t} + t^n k\frac{Q}{RT^2}\frac{dT}{dt} = \chi\left(\frac{n}{t} + \frac{Q}{RT^2}\frac{dT}{dt}\right) \tag{6}$$

or:

$$\frac{1}{\chi}\frac{d\chi}{dt} = \left(\frac{n}{t} + \frac{Q}{RT^2}\frac{dT}{dt}\right) \tag{7}$$

In the case of linear heating:

$$T = T_0 + \beta t \; and \; \frac{dT}{dt} = \beta \tag{8}$$

Equation (7) can be re-written in the form:

$$\frac{1}{\chi}\frac{d\chi}{dt} = \frac{d\chi}{dT}\frac{dT}{dt} = \beta\frac{d\chi}{dT} = \left(\frac{n}{(T-T_0)/\beta} + \frac{Q}{RT^2}\beta\right) = \beta\left(\frac{n}{(T-T_0)} + \frac{Q}{RT^2}\right) \tag{9}$$

It can be seen that the sintering rate $\frac{d\chi}{dt}$ depends on the heating rate (β) (i.e., the higher heating rate provides the higher sintering rate). However, the derivative of the densification function vs. temperature (i.e., $\frac{d\chi}{dT}$) does not depend on the heating rate (β):

$$\frac{d\chi}{dT} = \chi\left(\frac{n}{(T-T_0)} + \frac{Q}{RT^2}\right) \tag{10}$$

Analysis of the kinetic curves during the preheating stage (Figure 3) implies that $\chi = \chi(t)$ dependence with high accuracy can be fitted by linear function for both considered media (see Figure S2). The average $\frac{d\chi}{dt}$ was $(1.0 \pm 0.1) \times 10^{-3}$ s^{-1} and $(3.1 \pm 0.4) \times 10^{-3}$ s^{-1} for Cu + Cr and Cu/Cr media, respectively. Thus, in the preheating stage, the sintering rate for Cu/Cr media was much higher than that for the Cu + Cr mixture. It is worth noting that average values of $\frac{d\chi}{dt}$ recorded for both mixtures during the non-isothermal stage of sintering (~0.01–0.1 s^{-1}) were much higher than those observed during the isothermal stage (~10^{-4} s^{-1}).

Additional experiments were conducted for both materials with a heating rate of 5 K/min up to a maximum temperature of 973 K (see Table S1). Typical consolidation curves are shown in Figure S3. Again, relative densification rates for mechanically induced media appeared to be four times higher than for the conventional Cu + Cr mixture. However, the average $\frac{d\chi}{dt}$ in the preheating stage was smaller compared to those for experiments with 100 K/s (see also Table 1), while $\frac{d\chi}{dT}$ values, as predicted by Equation (10), were close to each other at 3.1./3.34 and 1.0/0.88 (see Table 1).

Furthermore, by integrating (10) for some temperature range (T^*, T), we may obtain the following relationship:

$$ln\chi\,|_{\chi^*}^{\chi} = ln\frac{\chi}{\chi^*} = nln\left(\frac{T}{T_0} - 1\right)\,|_{T^*}^{T} - \frac{Q}{R}\frac{1}{T}\,|_{T^*}^{T} = ln\left(\frac{T-T_0}{T^*-T_0}\right)^n + \frac{Q}{R}\left(\frac{1}{T^*} - \frac{1}{T}\right) \tag{11}$$

Equation (11) allows us to calculate the apparent activation energy Q by using data obtained during the preheating stage of the sintering process:

$$Q = \frac{R}{\left(\frac{1}{T^*} - \frac{1}{T}\right)} ln\left[\frac{\chi}{\chi^*}\left(\frac{T^*-T_0}{T-T_0}\right)^n\right] \tag{12}$$

Specifically, we assumed that parameter n was undependable on the heating conditions (isothermal and nonisothermal) and used n values obtained for the isothermal stage to analyze the preheating stage kinetics. In this case, by best fitting the $1/\chi \cdot (d\chi/dt) = F(1/T)$ curve, one can obtain the value for the apparent activation energy (see, for example, Figure S4). For the conventional Cu + Cr mixture, we obtained $Q_{Cu+Cr} = 125 \pm 10$ kJ/mol, while Q for the nanostructured Cu/Cr particles was $Q_{Cu/Cr} = 54 \pm 5$ kJ/mol. It is important that these values are in good agreement with those calculated for isothermal conditions.

The following conclusions can be made based on the above experimental findings:

(i) Under the investigated conditions, the sintering rates for the mechanically induced composite Cu/Cr particles were 2–4 times higher compared to that for the conventional Cu + Cr mixtures during both the isothermal and nonisothermal stages;
(ii) The apparent sintering activation energy for the Cu/Cr powder was approximately twice lower than that for the Cu + Cr mixture;
(iii) The sintering rate was much faster in the preheating stage compared to the isothermal stage for both mixtures; and
(iv) The higher heating rate resulted in a higher consolidation rate.

The latter conclusion suggested that we performed the sintering at extremely high heating rates (i.e., under, so-called, flash SPS conditions).

3.2. Flash Spark Plasma Sintering: Kinetics

The FSPS involves several stages. In the first stage, the powder mixture is relatively slowly (100 K/min) preheated to ~473 K. In the second stage, the current through the C–Cr media was rapidly (~10 s) increased to a value in the range of 450–685 A, leading to an extremely fast heating of the sample. The total process duration from the increase of the electrical current to its complete termination was 15 s.

It was not possible to accurately measure the rate of temperature change (β) during the second stage, thus we could only estimate this value based on the accurately measured values of the maximum reached temperatures. Such estimations showed that during FSPS, the heating rate β was in the range of 900–3000 K/min (i.e., up to 50 K/s), which was 10–30 times faster than the preheating rate (100 K/min) used during conventional SPS process.

Table 2 represents the final density (Δ_f) of the Cu/Cr specimens after FSPS with 15 s FSPS time. It can be seen that Δ_f for all conditions was larger than that for conventional SPS with a 10 min dwell time (for comparison some SPS data are also shown in Table 2).

Table 2. Structural characteristics of Cu/Cr materials consolidated by various SPS routes.

Mode	Sintering Condition		Relative Density (%)	The Relative Area of the Cu-Rich Phase (%)	The Size of Cr-Rich Particles (μm^2)
FSPS	40 K/s 698/15 s	Plan A	96.1 ± 0.4	4.3 ± 0.3	0.024 ± 0.01
		Plan B	97.1 ± 0.3	14.5 ± 0.6	0.05 ± 0.025
	45 K/s 748/15 s	Plan A	96.1 ± 0.4	4.3 ± 0.3	0.024 ± 0.01
		Plan B	97.5 ± 0.4	19.7 ± 0.9	0.93 ± 0.07
	50 K/s 818/15 s	Plan A	98.9 ± 0.1	38.3 ± 1.2	0.86 ± 0.6
		Plan B	99.3 ± 0.2	45.4 ± 2.6	2.13 ± 0.7
SPS	100 K/min 973 K/10 min	Plan A	96.5 ± 0.3	17.2 ± 0.9	0.13 ± 0.06
	5 K/min 973 K/10 min	Plan A	94.5 ± 0.2	22.6 ± 0.4	0.21 ± 0.13

The typical FSPS kinetics (615 A/15 s) curves for Cu + Cr and Cu/Cr media are shown in Figure 5a. The estimation implies that average consolidation rates in terms of $d\chi/dt$ were 0.065 s^{-1} and 0.05 s^{-1} for the Cu/Cr and Cu + Cr samples, respectively, while the maximum recorded $d\chi/dt$ was correspondingly around 0.14 s^{-1} and 0.12 s^{-1}. Thus, these average values were 20 and 50 times higher than those observed for SPS conditions with a 100 K/min heating rate. It is worth noting that these values are in qualitative agreement with Equation (9), which suggests that $d\chi/dt$ is proportional to the heating rate. However, the difference in $d\chi/dt$ between the mechanically induced composite particles and conventional Cu + Cr mixture was less under FSPS compared to the SPS conditions (see also Table 1).

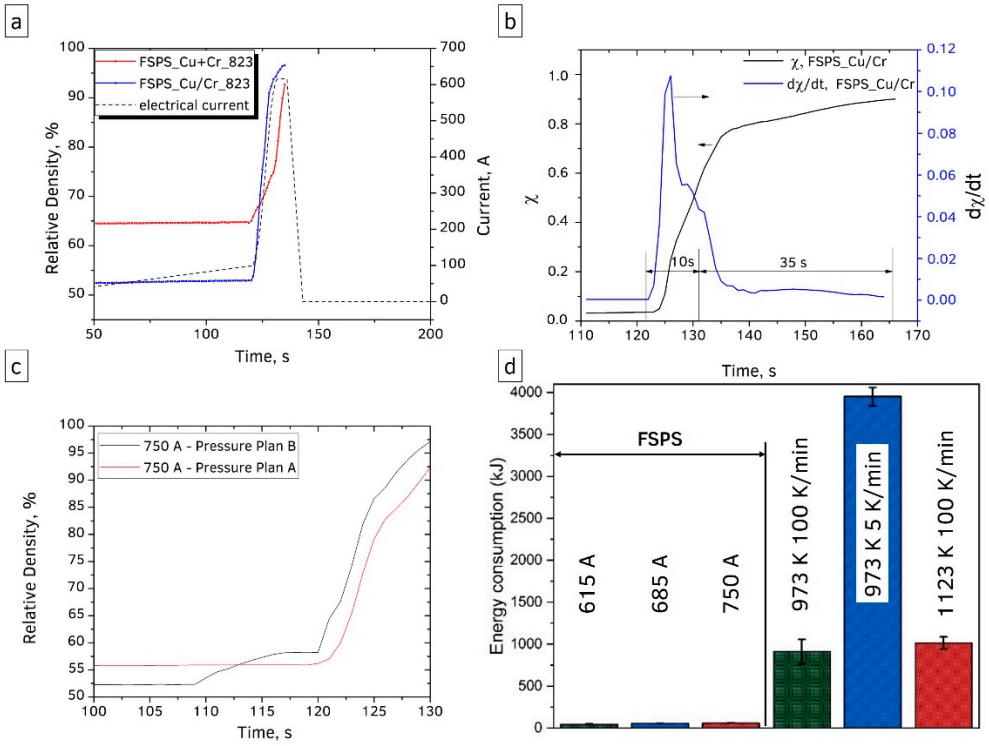

Figure 5. (**a**) Effect of high energy ball milling on the densification of samples fabricated by flash spark plasma sintering (FSPS). (**b**) Kinetics of FSPS consolidation of Cu/Cr media. (**c**) Effect of applied pressure. (**d**) Energy consumption for different sintering routes.

To compare the densification rates during rapid current change and constant current stages, a special set of experiments was conducted with relatively low maximum current (450 A/45 s) and relatively long (35 s) constant current stage (Figure 5b). It can be seen that the maximum consolidation rate of ~0.1 s^{-1} was observed during the first 4 s of the rapid current increase stage (total duration 10 s), while $d\chi/dt$ dropped (3–5) $\times$ 10^{-3} s^{-1} values at the constant current stage (35 s duration). The latter values are comparable with those reported above on the preheating stage for conventional SPS. This effect can be explained by the fact that upon reaching constant current, the temperature continued to grow (see Figure S5). At the end of a total 45 s of sintering, essentially complete consolidation was achieved.

It was also shown that if the load was applied just before the increase of electrical current (750 A/15 s), the final density of the materials was higher (Figure 5c). It is probably related to the better compressibility of the Cu/Cr particles at 573 K compared to room temperature. Indeed, as can be seen (Figure 5c), the difference between the initial densities of samples treated via plan A ($\Delta_0{}^A$ = 55.85) and B ($\Delta_0{}^B$ = 52.35) was 3.5% and it did not change during the preheating stage up to 573 K. However, when the load was applied to sample B (t = 109 s), in 10 s, its density surpassed that for sample A, which led to higher final density after the current was increased to 750 A. Finally, Figure 5d illustrates the obvious conclusion that FSPS allows for significant savings in the amount of energy for the fabrication of the alloys.

The following conclusions can be outlined:

(i) Under FSPS conditions, the observed maximum consolidation rates were 20–30 times higher than that for conventional SPS with a heating rate of 100 K/min;

(ii) The measured rate for temperature change $\beta = dT/dt$ during FSPS appeared to be in the range of 900–3000 K/min, and hence the extremely rapid consolidation rates can be explained just by an increase of the β (see Equation (9)). It implies that the mass

transport mechanism, which is responsible for the variation in the densification function with temperature $\frac{d\chi}{dT}$ remained the same; and

(iii) The above features, make FSPS an efficient approach for fabrication of the alloys. The load application schedule can be one more parameter for optimization of the consolidation process.

3.3. Microstructure of the Pseudo-Alloys

Typical microstructures of the Cu/Cr-based materials fabricated by conventional SPS with different temperature-time schedules are shown in Figure 6. It can be seen that for all considered conditions, the microstructure consisted of relatively large composite Cu/Cr grains and Cu layers (light phase). The size of the grains was close to the size of the mechanically-induced Cu/Cr particles (10–20 μm). The microstructures shown in Figure 6a,b (100 K/min up to 973 K with zero dwell time) suggest that Cu layers formed during the preheating stage. A comparison with Figure 6c,d (100 K/min up to 973 K with 10 s dwell time) implies that the thickness of the Cu layers increases during the isothermal stage, while the size of the Cr grains (dark phase) in the composite grains remained essentially unchanged. Finally, slower heating rate (5 K/min) leads to qualitatively similar microstructures (Figure 6e,f), but with thicker (up to 5 μm) Cu layers.

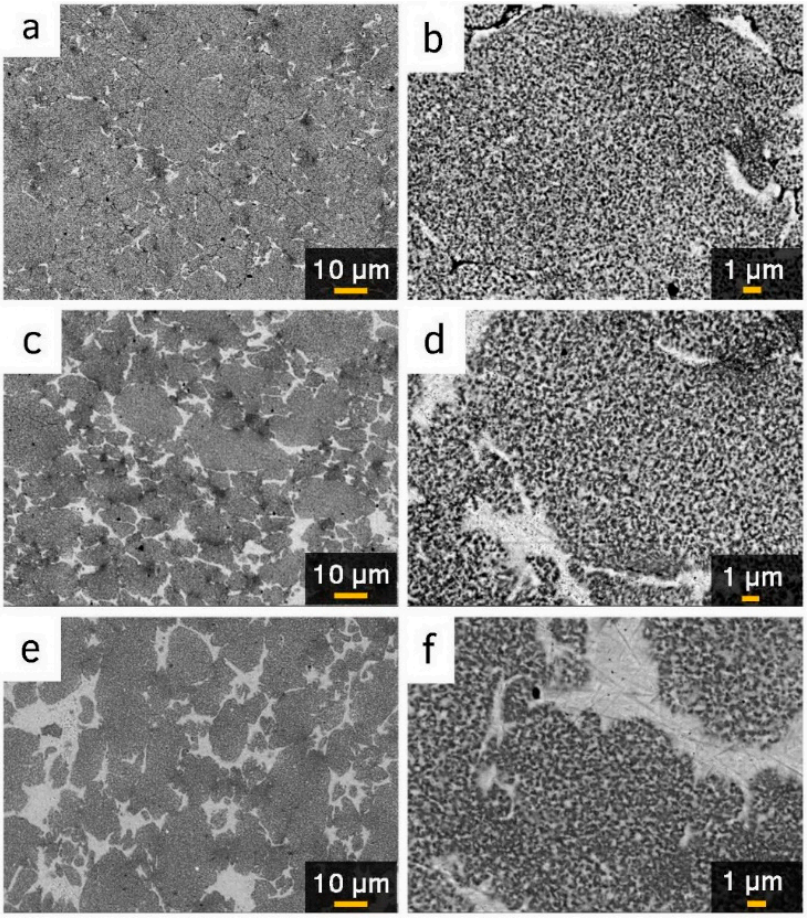

Figure 6. Effect of heating rate on the microstructure of Cu/Cr powder sintered at 973 K: (**a**,**b**) 100 K/min without dwelling time; (**c**,**d**) 100 K/min with 10 min dwelling time; (**e**,**f**) 5 K/min with 10 min dwelling time.

The microstructures of the alloys obtained after SPS of the conventionally mixed Cu + Cr particles are shown in Figure 7. It can be seen that the microstructures were much coarser (Cr grains were in the range of 10–25 μm) that those for the Cu/Cr-based materials (submicron Cr grains). The samples fabricated at 973 K (Figure 7a–d) had large pores

(average density was 85 ± 3%) and cracks along the interphase between the Cr grains. A relatively high temperature (1123 K) is required to fabricate a material (Figure 7e,f) with a relative high density (94 ± 3%).

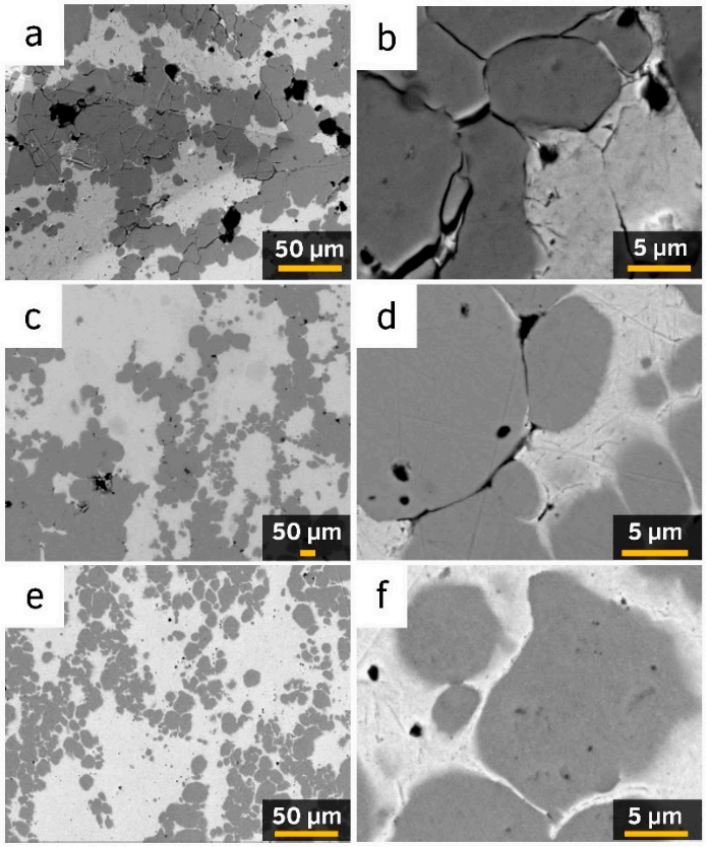

Figure 7. Effect of heating rate on the microstructure of conventional Cu + Cr powder sintered with a 10 min dwell time: (**a**,**b**) 100 K/min at 973 K; (**c**,**d**) 5 K/min at 973 K; (**e**,**f**) 100 K/min 1023 K.

The FSPS_Cu/Cr_823, for which the maximum reached temperature was 823 K, had a microstructure (Figure 8a,b) similar to that of the SPS_Cu/Cr with a maximum temperature of 923 K, and involved nanostructured Cu/Cr grains and thin Cu layers. However, when the maximum reached temperature was 1043 K, two new features could be outlined (Figure 8c,d): (i) homogenization of the microstructure on the micron scale level (compare Figures 8a and 8c), and (ii) the growth of Cr grains up to 1 µm in size.

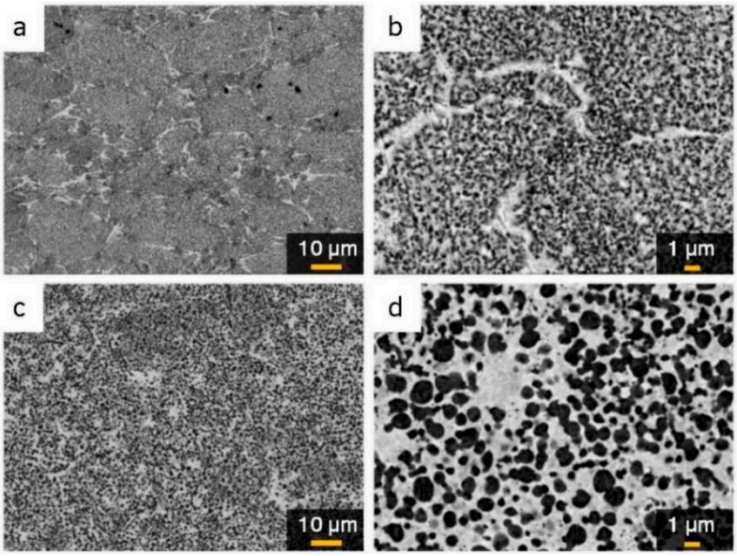

Figure 8. Typical microstructures of the materials fabricated under different FSPS conditions: (**a**,**b**) sample FSPS_Cu/Cr_823K (450A, 25 s) and (**c**,**d**) FSPS_Cu/Cr_1043K (450 A, 45 s).

Comparison of the microstructures of the FSPS_Cu+Cr_698K and FSPS_Cu/Cr_818 K samples is shown in Figure 9. It can be seen that the Cu + Cr alloy (a,b) after 15 s of heat treatment had similar features obtained after SPS with 10 min of dwell time at 923 K. The Cr/Cu sample (c,d) had the highest final density (~99%; Table 1), which was reached only after 15 s of the consolidation process at T_{max} = 818 K. The Cu/Cr alloy again possessed a much finer structure compared to that for the Cu + Cr alloy. The microstructural characteristics of the alloys obtained under different consolidation conditions are summarized in Table 2. The following general conclusions can be outlined:

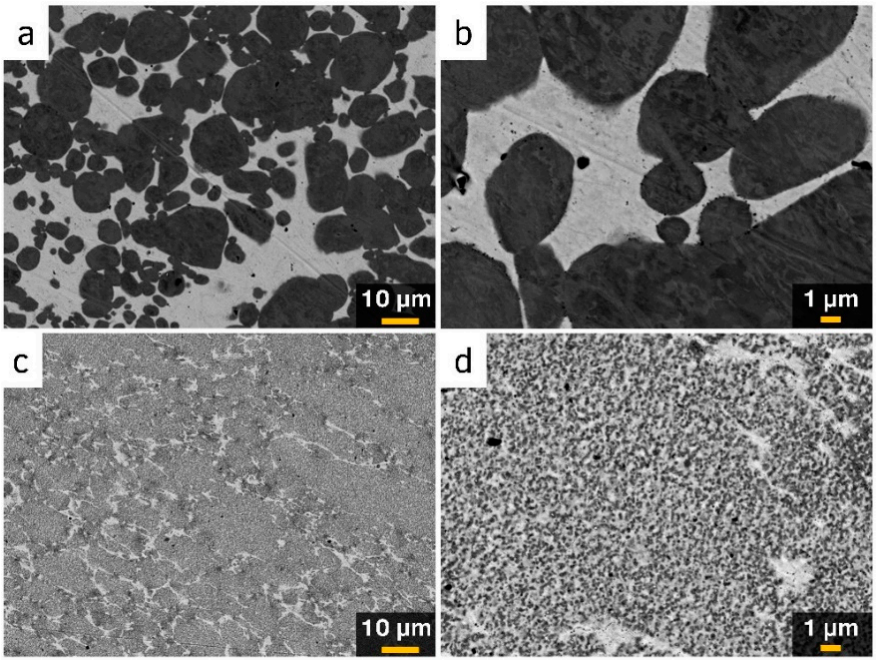

Figure 9. Typical microstructures of materials (**a**,**b**); Cu + Cr powder after FSPS; and (**c**,**d**) Cu/Cr after a FSPS maximum temperature of 818 K and total duration of 15 s.

After a short (~15 s) FSPS process, the formed alloy's microstructures were similar to that after long term (10 min) conventional SPS consolidation;

Pseudo-alloys fabricated from the nanostructured composite Cr/Cu particles possessed a much finer microstructure compared to those obtained from the Cu + Cr mixture

3.4. Properties

Some mechanical, electrical, and thermal properties of the consolidated Cr/Cr and Cu + Cr alloys are summarized in Tables 3 and 4, respectively.

Table 3. Some properties of the Cu/Cr nanostructured pseudo-alloys.

Sample	Plan for Applied Pressure	Electrical Resistivity mΩ·cm/Conductivity % IACS	Thermal Diffusivity mm^2/s	Macro Hardness GPa	Micro Hardness GPa	Elastic Modulus GPa
SPS_ 5_973	A	7.7 ± 0.4/22	28.4 ± 0.1	4.6 ± 0.2	4.4 ± 0.5	244 ± 20
SPS_100_973	A	7.3 ± 0.4/24	27.0 ± 0.1	5.2 ± 0.8	5.2 ± 1.2	210 ± 15
SPS_100_1123	A	6.2 ± 0.1/28	32.8 ± 0.2	4.4 ± 0.3	4.1 ± 0.5	203 ± 11
FSPS_698	A	7.6 ± 0.2/23	29.6 ± 0.2	5.0 ± 0.2	4.3 ± 0.2	238 ± 19
	B	7.8 ± 0.2/22	30.0 ± 0,1	3.3 ± 0.8	3.4 ± 0.2	202 ± 22
FSPS_748	A	7.9 ± 0.2/22	30.5 ± 0.1	5.2 ± 0.4	5.3 ± 0.7	228 ± 45
	B	8.8 ± 0.2/20	28.4 ± 0.2	4.0 ± 1.0	3.4 ± 0.3	214 ± 13
FSPS_818	A	8.9 ± 0.3/20	30.0 ± 0.2	3.9 ± 0.4	4.3 ± 0.2	197 ± 24
	B	7.5 ± 0.1/23	30.8 ± 0.2	3.8 ± 0.2	4.5 ± 0.2	201 ± 20

Table 4. Some properties of the Cu–Cr pseudo-alloys.

Sample	Electrical Resistivity mΩ·cm/Conductivity % IACS	Thermal Diffusivity mm^2/s	Macro Hardness GPa	Micro Hardness GPa	Elastic Modulus GPa
SPS_5_973	6.1 ± 0.3/28	43.9 ± 0.3	0.71 ± 0.04	1.3 ± 0.1	136 ± 15
SPS_100_973	6.9 ± 0.3/25	37.0 ± 0.5	0.51 ± 0.02	1.0 ± 0.1	–
SPS_100_1123	5.7 ± 0.2/30	42.2 ± 0.6	1.05 ± 0.05	–	–

It can be seen that the electrical resistivity of the Cu/Cr nanostructured alloys was ~7.5 mΩ·cm, which was slightly above than that for the Cu + Cr alloys of ~6.5 mΩ·cm. Correspondingly, the thermal diffusivity of the nano-alloys (~30 mm^2/s) was lower (~40 mm^2/s for the micro-scale alloys). All reported mechanical properties of the Cu/Cr materials were much higher than those for Cu + Cr. It is worth noting that the Young modulus for Cu/Cr alloys was in the range reported for chromium (245–285 GPa), while for Cu + Cr, it was in the order for pure cooper (130 GPa) [35]. In addition, the Cu/Cr materials were 4–5 times harder than the Cu + Cr opponents.

All of the above trends can be explained by the significant differences in the microstructures of the alloys. It can be seen (compare Figures 6, 7 and 9) that regardless of the consolidation method, the Cu/Cr materials primarily consisted of nanostructured Cu/Cr grains, where the metals were mixed on a sub-micron level, while the Cu + Cr alloys exhibited large (20 μm) grains of Cr immersed into the Cu-matrix.

The nanostructured Cu/Cr grains dictate high hardness and elastic modulus. A more developed percolation copper net in the Cu + Cr alloys led to the higher electrical and thermal conductivities. Finally, it is important that by using the rapid energy and time saving FSPS approach, one may obtain alloys with similar microstructures and thus properties such as those consolidated by the relatively long-term conventional SPS method.

4. Conclusions

The SPS kinetics for Cu–Cr alloys were investigated for heating rate in the range of 5–3000 K/min. It was shown that under FSPS (i.e., heating rate ~10^3 K/min), the observed maximum consolidation rates were 20–30 times higher than that for the SPS with a heating rate of 100 K/min. However, the analysis showed that such rapid consolidation could be

explained just by the increase of the β (see Equation (9)), which suggests that the mass transport mechanism does not change. The latter is an important fundamental conclusion that allows for analysis of FSPS using kinetic parameters obtained under conventional SPS.

In contrast, it was demonstrated that by changing the microstructure of the media, one may significantly vary the SPS kinetics. Indeed, under similar conditions, the sintering rates for mechanically induced composite Cu/Cr particles were 2–4 times higher compared to those for conventional Cu + Cr mixtures. The latter conclusion was valid for both isothermal and nonisothermal consolidation stages. This effect can be explained by the different mass transport mechanisms (i.e., the surface diffusion for nanocomposite particles and the volume diffusion for conventional mixture of metals).

The pseudo-alloys fabricated from the nanostructured composite Cr/Cu particles possessed a much finer microstructure compared to those obtained from the Cu + Cr mixture. This effect leads to much higher mechanical properties of the Cu/Cr alloys. Finally, the microstructures and properties of the pseudo-alloys obtained from Cu/Cr particles after a short (~15 s) FSPS process were similar to those fabricated during relatively long-term (10 min) conventional SPS consolidation. The above features make FSPS an efficient approach for production of the alloys.

Supplementary Materials: The following are available online at https://www.mdpi.com/2075-4701/11/1/141/s1, Figure S1: Sintering profiles for different consolidation schemes: (**a**) SPS; (**b**) FSPS Sintering conditions for different consolidation schemes, Figure S2: Kinetic curves during the preheating stage for: conventional Cu + Cr mixture (**a**,**b**); and Cu/Cr particles (**c**,**d**) (SPS conditions: heating rate 100 K/min, Plan A). Figure S3: The dependences of relative density vs temperature for: (**a**) conventional Cu + Cr mixture; (**b**) and Cu/Cr particles (SPS conditions: Tmax = 973 K; heating rate 5 K/min, Plan A). Figure S4: Estimation of the activation energy (Q) of sintering during non-isothermal stage for (a) Cu + Cr mixture and (b) fore Cu/Cr nanostructured particles. Figure S5: The dependences of current and temperature vs temperature for FSPS; Table S1: Sintering conditions for different consolidation schemes.

Author Contributions: Conceptualization, A.S.M., M.A., and K.V.K.; Methodology, A.S.M., K.V.K., M.A., and D.O.M.; Validation, A.S.M., K.V.K., and D.O.M.; Formal analysis, A.S.M., K.V.K., and M.A.; Investigation, K.V.K., M.A., and I.S.; Writing—original draft preparation, A.S.M., M.A., K.V.K., and D.O.M.; Project administration, A.S.M. and D.O.M. All authors have read and agreed to the published version of the manuscript.

Funding: This research was supported by the Ministry of Science and Higher Education of the Russian Federation (No. K2-2020-015).

Institutional Review Board Statement: Not applicable.

Informed Consent Statement: Not applicable.

Data Availability Statement: The data presented in this study are available in Supplementary Materials.

Acknowledgments: The authors gratefully acknowledge financial support from the Ministry of Science and Higher Education of the Russian Federation in the framework of Increase Competitiveness Program of NUST MISiS (No. K2-2020-015), implemented by a governmental decree dated 16 March 2013 (No. 211).

Conflicts of Interest: The authors declare no conflict of interest.

References

1. Kumar, A.; Jayasankar, K.; Debata, M.; Mandal, A. Mechanical alloying and properties of immiscible Cu-20 wt.% Mo alloy. *J. Alloys Compd.* **2015**, *647*, 1040–1047. [CrossRef]
2. Mousavi, T.; Dai, J.; Bazarnik, P.; Pereira, P.H.R.; Huang, Y.; Lewandowska, M.; Langdon, T.G. Fabrication and characterization of nanostructured immiscible Cu–Ta alloys processed by high-pressure torsion. *J. Alloys Compd.* **2020**, *832*, 155007. [CrossRef]
3. Kuskov, K.V.; Sedegov, A.S.; Novitskii, A.P.; Nepapushev, A.A.; Moskovskikh, D.O.; Shkodich, N.F.; Rogachev, A.S.; Mukasyan, A.S. Influence of chromium in nanocrystalline copper–chromium pseudoalloy on its structure and properties. *Nanotechnol. Russ.* **2017**, *12*, 40–48. [CrossRef]

4. Shkodich, N.F.; Rogachev, A.S.; Mukasyan, A.S.; Moskovskikh, D.O.; Kuskov, K.V.; Schukin, A.S.; Khomenko, N.Y. Preparation of copper–molybdenum nanocrystalline pseudoalloys using a combination of mechanical activation and spark plasma sintering techniques. *Russ. J. Phys. Chem. B* **2017**, *11*, 173–179. [CrossRef]
5. Sanin, V.V.; Filonov, M.R.; Yukhvid, V.I.; Anikin, Y.A.; Ikornikov, D.M. Production of the 70% Cu–30% Fe Alloy by SHS Metallurgy and Electrometallurgy: Comparative Analysis of Microstructures. *Russ. J. Non-Ferrous Met.* **2020**, *61*, 119–125. [CrossRef]
6. Loginov, P.A.; Vorotilo, S.; Sidorenko, D.A.; Lopatina, Y.V.; Okubayev, A.; Shvyndina, N.V.; Levashov, E.A. Influence of Ti and TiH2 Additives on the Structure and Properties of Copper Alloys for Diamond Cutting Tools. *Russ. J. Non-Ferrous Met.* **2020**, *61*, 429–435. [CrossRef]
7. Slade, P.G. *The Vacuum Interrupter: Theory, Design and Application*, 1st ed.; CRC Press: Boca Raton, FL, USA, 2007; ISBN 1420008595.
8. Szemkus, S.; Kempf, B.; Jahn, S.; Wiehl, G.; Heringhaus, F.; Rettenmayr, M. Laser additive manufacturing of contact materials. *J. Mater. Process. Technol.* **2018**, *252*, 612–617. [CrossRef]
9. Chen, Y.; Ren, S.; Zhao, Y.; Qu, X. Microstructure and properties of CuCr alloy manufactured by selective laser melting. *J. Alloys Compd.* **2019**, *786*, 189–197. [CrossRef]
10. Momeni, S.; Guschlbauer, R.; Osmanlic, F.; Körner, C. Selective electron beam melting of a copper-chrome powder mixture. *Mater. Lett.* **2018**, *223*, 250–252. [CrossRef]
11. Fang, Q.; Kang, Z.; Gan, Y.; Long, Y. Microstructures and mechanical properties of spark plasma sintered Cu–Cr composites prepared by mechanical milling and alloying. *Mater. Des.* **2015**, *88*, 8–15. [CrossRef]
12. Fang, Q.; Kang, Z. An investigation on morphology and structure of Cu–Cr alloy powders prepared by mechanical milling and alloying. *Powder Technol.* **2015**, *270*, 104–111. [CrossRef]
13. Sheibani, S.; Heshmati-Manesh, S.; Ataie, A.; Caballero, A.; Criado, J.M. Spinodal decomposition and precipitation in Cu–Cr nanocomposite. *J. Alloys Compd.* **2014**, *587*, 670–676. [CrossRef]
14. Zhao, Q.; Shao, Z.; Liu, C.; Jiang, M.; Li, X.; Zevenhoven, R.; Saxén, H. Preparation of Cu–Cr alloy powder by mechanical alloying. *J. Alloys Compd.* **2014**, *607*, 118–124. [CrossRef]
15. Shi, K.; Xue, L.; Yan, Y.; Shen, T. Effects of mechanical alloying parameters on the microstructures of nanocrystalline Cu-5 wt% Cr alloy. *J. Wuhan Univ. Technol. Sci. Ed.* **2013**, *28*, 192–195. [CrossRef]
16. Pang, Y.; Xia, C.; Wang, M.; Li, Z.; Xiao, Z.; Wei, H.; Sheng, X.; Jia, Y.; Chen, C. Effects of Zr and (Ni, Si) additions on properties and microstructure of Cu–Cr alloy. *J. Alloys Compd.* **2014**, *582*, 786–792. [CrossRef]
17. Sheibani, S.; Heshmati-Manesh, S.; Ataie, A. Influence of Al2O3 nanoparticles on solubility extension of Cr in Cu by mechanical alloying. *Acta Mater.* **2010**. [CrossRef]
18. Zhao, L.; Chen, X.; Liu, P.; Li, W.; Ma, F.; He, D.; Li, J. Effect of yttrium on the electrical and mechanical properties of in situ synthesized CNTs/CuCr composites. *J. Mater. Res.* **2019**. [CrossRef]
19. Dobatkin, S.V.; Gubicza, J.; Shangina, D.V.; Bochvar, N.R.; Tabachkova, N.Y. High strength and good electrical conductivity in Cu–Cr alloys processed by severe plastic deformation. *Mater. Lett.* **2015**, *153*, 5–9. [CrossRef]
20. Kuskov, K.V.; Rogachev, A.S.; Vadchenko, S.G.; Shkodich, N.F.; Rouvimov, S.; Shchukin, A.S.; Illarionova, E.V.; Kudryashov, V.A.; Mukasyan, A.S. Resistance of microcrystalline and nanocrystalline Cu/Cr pseudo-alloys to vacuum discharge. *J. Alloys Compd.* **2018**, *750*, 811–818. [CrossRef]
21. Wei, X.; Yu, D.; Sun, Z.; Yang, Z.; Song, X.; Ding, B. Arc characteristics and microstructure evolution of W–Cu contacts during the vacuum breakdown. *Vacuum* **2014**, *107*, 83–89. [CrossRef]
22. Lahiri, I.; Bhargava, S. Compaction and sintering response of mechanically alloyed Cu–Cr powder. *Powder Technol.* **2009**, *189*, 433–438. [CrossRef]
23. Diatta, J.; Antou, G.; Pradeilles, N.; Maître, A. Numerical modeling of spark plasma sintering—Discussion on densification mechanism identification and generated porosity gradients. *J. Eur. Ceram. Soc.* **2017**, *37*, 4849–4860. [CrossRef]
24. Klinger, L.; Rabkin, E. Sintering of spherical particles of two immiscible phases controlled by surface and interphase boundary diffusion. *Acta Mater.* **2013**, *61*, 2607–2616. [CrossRef]
25. Olevsky, E.; Froyen, L. Constitutive modeling of spark-plasma sintering of conductive materials. *Scr. Mater.* **2006**, *55*, 1175–1178. [CrossRef]
26. Hu, Z.-Y.; Zhang, Z.-H.; Cheng, X.-W.; Wang, F.-C.; Zhang, Y.-F.; Li, S.-L. A review of multi-physical fields induced phenomena and effects in spark plasma sintering: Fundamentals and applications. *Mater. Des.* **2020**, *191*, 108662. [CrossRef]
27. Saheb, N.; Iqbal, Z.; Khalil, A.; Hakeem, A.S.; Al Aqeeli, N.; Laoui, T.; Al-Qutub, A.; Kirchner, R. Spark Plasma Sintering of Metals and Metal Matrix Nanocomposites: A Review. *J. Nanomater.* **2012**, *2012*, 1–13. [CrossRef]
28. Guillon, O.; Gonzalez-Julian, J.; Dargatz, B.; Kessel, T.; Schierning, G.; Räthel, J.; Herrmann, M. Field-assisted sintering technology/spark plasma sintering: Mechanisms, materials, and technology developments. *Adv. Eng. Mater.* **2014**, *16*, 830–849.
29. Chaim, R.; Chevallier, G.; Weibel, A.; Estournès, C. Grain growth during spark plasma and flash sintering of ceramic nanoparticles: A review. *J. Mater. Sci.* **2018**, *53*, 3087–3105. [CrossRef]
30. Manière, C.; Lee, G.; Olevsky, E.A. All-Materials-Inclusive Flash Spark Plasma Sintering. *Sci. Rep.* **2017**, *7*, 15071. [CrossRef]
31. Torosyan, K.S.; Sedegov, A.S.; Kuskov, K.V.; Abedi, M.; Arkhipov, D.I.; Kiryukhantsev-Korneev, P.V.; Vorotilo, S.; Moskovskikh, D.O.; Mukasyan, A.S. Reactive, nonreactive, and flash spark plasma sintering of Al_2O_3/SiC composites—A comparative study. *J. Am. Ceram. Soc.* **2020**, *103*, 520–530. [CrossRef]

32. Tikkanen, M.H.; Yläsaari, S. On the Mechanisms of Sintering. In *Modern Developments in Powder Metallurgy*; Springer: Boston, MA, USA, 1966; pp. 297–309.
33. Thümmler, F.; Thomma, W. The sintering process. *Metall. Rev.* **1967**, *12*, 69–108. [CrossRef]
34. Demirskyi, D.; Agrawal, D.; Ragulya, A. Densification kinetics of powdered copper under single-mode and multimode microwave sintering. *Mater. Lett.* **2010**, *64*, 1433–1436. [CrossRef]
35. Freund, L.B.; Suresh, S. *Thin Film Materials: Stress, Defect Formation and Surface Evolution*; Illustrated edition; Cambridge University Press: Cambridge, UK, 2003; ISBN 9780511165658.